






Cite this: *Mater. Adv.*, 2021,  
2, 7431

# An organic–inorganic hybrid double perovskite-type cage-like crystal (MA)<sub>2</sub>KBiCl<sub>6</sub> (MA = methylammonium cation) with dielectric switching behavior†

Lin Xiang, Yi-Fang Huang, Yan Feng, Na Wang, Rong-Meng Liao, Le-Ping Miao,\*  
Jian-Rong Li,  Heng-Yun Ye  and Chao Shi  \*

An organic–inorganic hybrid double perovskite-type cage-like crystal, (MA)<sub>2</sub>KBiCl<sub>6</sub> (MA = methylammonium cation, **1**), was synthesized. It undergoes structural phase transitions at 336/326 K (heating/cooling). Variable-temperature single-crystal structural analyses reveal that the change of the dynamics of the MA and the deformation of the anionic cage-like framework contribute to the structural phase transition. This order–disorder transition of the MA causes dielectric transitions between the low- and high-dielectric states, making it a type of switchable dielectric material. Furthermore, dielectric anisotropic properties and reversibility of the dielectric switching of this crystal under temperature stimuli are also identified. The results reveal that hybrid double perovskite-related halides provide a promising platform for achieving switchable dielectric properties, and more hybrid perovskites can be prepared by using different organic amines as the A-site cation.

Received 5th August 2021,  
Accepted 13th September 2021

DOI: 10.1039/d1ma00691f

rsc.li/materials-advances

## Introduction

Hybrid perovskites are ABX<sub>3</sub>-type materials with the same structure as that of CaTiO<sub>3</sub>, known as a perovskite structure.<sup>1</sup> In hybrid perovskites, the A-site metal ion is generally changed to a molecular cation, meanwhile, the X-site oxygen ion is replaced by an anionic bridging ligand (X = H<sub>2</sub>POO<sup>−</sup>,<sup>2</sup> HCOO<sup>−</sup>,<sup>3</sup> NO<sub>2</sub><sup>−</sup>,<sup>4</sup> halide ions,<sup>1,5</sup> CN<sup>−</sup>,<sup>6</sup> *etc.*), forming anionic cage-like host–guest structures. A further expansion is made by replacing the B-site metal ions with two different metal ions to give double perovskites (A<sub>2</sub>B'B''X<sub>6</sub>).<sup>7–9</sup> They displayed various technologically important properties, which are closely related to those of the perovskite structure. In recent years, hybrid perovskites have emerged as one of the fastest growing research fields in materials science.<sup>10,11</sup> These perovskites offer opportunities for combining attractive features of inorganic and organic systems within perovskite structures, leading to additional functions and/or novel properties.<sup>12,13</sup> As one of the most important properties of perovskite materials, the dielectric transition was also realized in hybrid perovskites.

The research in dielectric transition, which is a switchable dielectric constant, is increasingly motivated by both basic scientific concerns and fantastic potential applications in many electronic devices, ranging from sensors and actuators to switches and so on.<sup>14</sup> As one of the basic elements in electrical and electronic industries, dielectric materials are widely used as capacitors. For example, those with low-dielectric constants  $\epsilon'$  are used in integrated circuits and high dielectrics have use in applications of energy storage and device miniaturization. Among them, molecular-based species with switchable dielectric constant properties are of growing interest. Up to now, reversible switching of a dielectric constant has been extensively studied in single hybrid perovskites by electrochemical modification for their excellent reversibility and switchable dielectric constant. However, only scarce reports have been focused on double perovskites, especially those with high-temperature switchable dielectric performance.

In recent years, halide double perovskites have shown great advantages in realizing structural phase transitions.<sup>7–9</sup> Intriguing electrical properties, such as dielectric transitions, are mainly due to the structural changes from perfect cubic to highly twisted perovskite structures *via* disordering of the organic cations, displacements of the metal ions, and/or distortions of the anion octahedra. A very good example was reported by Cheetham *et al.*<sup>15</sup> The organic–inorganic hybrid double perovskite-type cage-like compound, (MA)<sub>2</sub>KBiCl<sub>6</sub>, shows characteristics that are very similar to the well-studied

Chaotic Matter Science Research Center, Jiangxi University of Science and Technology, Ganzhou 330000, Jiangxi, China. E-mail: miaoleping@seu.edu.cn, 15150517670@163.com

† Electronic supplementary information (ESI) available: Crystal morphology, IR spectrum, TGA curve and PXRD pattern. CCDC 2101468 and 2101469. For ESI and crystallographic data in CIF or other electronic format see DOI: 10.1039/d1ma00691f

(MA)PbX<sub>3</sub> (X = halide ion) perovskite.<sup>16</sup> So, even though the hybrid double perovskite (MA)<sub>2</sub>KBiCl<sub>6</sub> has been reported to show semiconducting properties,<sup>15</sup> it may have a switchable dielectric behavior that enables its wide use as the basic element in electrical and electronic industries. Herein, we report a study of a switchable dielectric constant in the halide double perovskite compound (MA)<sub>2</sub>KBiCl<sub>6</sub> (MA = methylammonium cation; **1**). The compound undergoes an order–disorder phase transition at 336/326 K (heating/cooling). Variable-temperature single-crystal structural analysis reveals that reorientational changes of the MA in the anionic cage mainly account for its dielectric transition.

## Experimental section

### Materials and methods

All chemicals of analytical grade were purchased from Sigma-Aldrich. None of the reagents needed further purification for synthesis. The title compound, (MA)<sub>2</sub>KBiCl<sub>6</sub> (MA = methylammonium cation; **1**), was not obtained by the reported method.<sup>15</sup> **1** was obtained *via* a solution–evaporation method in this paper. The hybrid double perovskite-type cage-like crystal was isolated as crystals by evaporation of the hydrochloric acid solution containing stoichiometric amounts of (MA)Cl, KCl, and BiCl<sub>3</sub>. The preparation procedure is as follows: an excessive hydrochloric acid solution (15 mL) containing (MA)Cl (2.66 g, 16 mmol), KCl (0.66 g, 8 mmol), and BiCl<sub>3</sub> (2.52 g, 8 mmol) was slowly evaporated at room temperature to yield colorless block crystals of **1** (yield 75%, based on BiCl<sub>3</sub>). Elemental analysis calcd (%) for **1**: C, 4.58; H, 2.30; N, 5.34. Found: C, 4.60; H, 2.31; N, 5.31.

### General characterization

Elemental analysis was carried out on a Vario MICRO (Germany) analyzer. The solid powder infrared spectrum was collected using a Thermo Scientific Nicolet iS10 FT-IR spectrometer with KBr pellets. Powder X-ray diffraction (PXRD) was collected on a Rigaku SmartLab X-ray diffractometer. Thermal gravimetric analysis was performed using an SDT-Q600 system (NETZSCH) in airflow. Differential scanning calorimetry (DSC) measurements were performed on a NETZSCH DSC 200F3 instrument with the temperature range of 293–373 K and a heating/cooling rate of 10 K min<sup>−1</sup>. The collection of variable-temperature single-crystal data was performed with Mo-K<sub>α</sub> radiation ( $\lambda = 0.71073$  Å) at 293 K and 373 K, respectively, on a Rigaku Saturn 924<sup>+</sup> diffractometer equipped with a Rigaku low-temperature device. The crystal structures were solved by direct methods and refined using the full-matrix method based on  $F^2$  using the SHELXL-2018 software package. Non-hydrogen atoms were refined anisotropically. Meanwhile, H atoms were located geometrically at idealized positions and refined using a “riding” model. The detailed crystallographic data of compound **1** is shown in Table 1. The crystalline-powdered samples and single-crystal samples with well-defined faces were sandwiched by silver conduction paste

Table 1 Crystallographic data of **1** at 293 K and 373 K

	<b>1</b>	<b>1</b>
<i>T</i> /K	293(2)	373(2)
Formula	C <sub>2</sub> H <sub>12</sub> N <sub>2</sub> KBiCl <sub>6</sub>	C <sub>2</sub> H <sub>12</sub> N <sub>2</sub> KBiCl <sub>6</sub>
CCDC	2101468	21014689
Formula weight	524.92	524.92
Crystal system	Trigonal	Cubic
Space group	$R\bar{3}m$	$Fm\bar{3}m$
<i>a</i> /Å	7.8314(2)	11.4524(3)
<i>b</i> /Å	7.8314(2)	11.4524(3)
<i>c</i> /Å	20.9786(7)	11.4524(3)
$\alpha$ /°	90	90
$\beta$ /°	90	90
$\gamma$ /°	120	90
<i>V</i> /Å <sup>3</sup>	1114.26(7)	1502.07(12)
<i>Z</i>	3	2
<i>D</i> <sub>calc</sub> /g cm <sup>−3</sup>	2.347	2.321
$\mu$ /mm <sup>−1</sup>	13.19	13.05
<i>F</i> (000)	726	968.1
$\theta$ range/°	2.9–30.9	3.1–30.3
Reflns collected	5787	1805
Independent reflns ( <i>R</i> <sub>int</sub> )	0.050	0.032
No. of parameters	20	26
<i>R</i> <sub>1</sub> <sup>a</sup> , <i>wR</i> <sub>2</sub> <sup>b</sup> [ <i>I</i> > 2σ( <i>I</i> )]	0.018	0.016
<i>R</i> <sub>1</sub> , <i>wR</i> <sub>2</sub> [all data]	0.040	0.031
GO	1.12	1.09
$\Delta\rho^c$ /e Å <sup>−3</sup>	0.76/−0.59	0.25/−0.44

<sup>a</sup>  $R_1 = \sum ||F_o| - |F_c|| / \sum |F_o|$ . <sup>b</sup>  $wR_2 = [\sum w(F_o^2 - F_c^2)^2 / \sum w(F_o^2)^2]^{1/2}$ .

<sup>c</sup> Maximum and minimum residual electron density.

between two parallel electrodes for complex dielectric constant measurements. Dielectric constant curves were measured on a Tonghui TH2828A analyzer by heating–cooling cycles in the frequency and temperature ranges of 500 Hz–1000 kHz and 293–363 K.

## Results and discussion

### Thermal analysis of **1**

Firstly, the pure phase of the polycrystalline samples of **1** was verified by PXRD (Fig. S1, ESI†). And then the polycrystalline samples were used in thermal gravimetric analysis which showed that **1** was stable below 500 K (Fig. S2, ESI†), and infrared (IR) spectroscopy was performed to detect the vibration absorption of chemical bonds or groups of compound **1**; the relative absorption band at 3000.79 cm<sup>−1</sup> indicated the –NH bond of **1** (Fig. S3, ESI†). The structural phase transition of **1** was confirmed by DSC measurements (Fig. 1). In the measured temperature range of 293–373 K, **1** shows reversible endo- and exothermic peaks. A pair of peaks appear above the room temperature at 336/326 K (heating/cooling), respectively, corresponding to a reversible phase transition. The thermal hysteresis is 10 K at a scanning rate of 10 K min<sup>−1</sup>. The entropy changes  $\Delta S$  are calculated from the measured enthalpy changes during the phase transitions with a value of 6.42 J mol<sup>−1</sup> K<sup>−1</sup> for **1**. According to the Boltzmann equation,  $\Delta S = R \ln N$ , the number of microscopic state changes *N* is roughly estimated to be 2.20, indicating that the phase transition is of the order–disorder type. To clarify the type of the phase transition of **1**, we evaluated the scanning rate dependence of the DSC measurements on compound **1** (Fig. S4, ESI†). The result shows that the



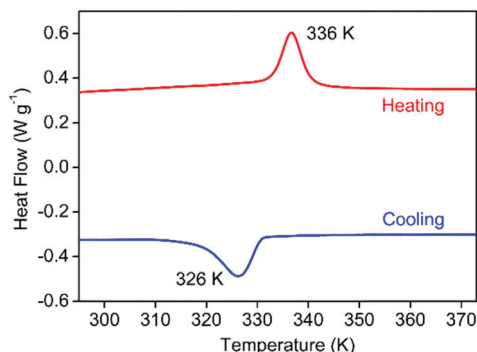


Fig. 1 DSC curve for **1** measured in the temperature range of 293–373 K.

$\Delta T$  of the phase transition increased as the scanning rate increased which indicates that the phase transition of **1** is of the first order type.<sup>17</sup> Furthermore, the variable-temperature powder XRD patterns were recorded, which verified the reversible phase transitions that responded to DSC (Fig. S5, ESI†).

### Crystal structures

The thermal-triggered phase transition was also evidenced by variable-temperature single-crystal structure analysis. As illustrated in Fig. 2, **1** adopts a typically  $A_2B'B''X_6$ -type three-dimensional (3D) perovskite structure, in which the cation is in the cage formed by an inorganic framework. Its inorganic framework is composed of the heterometal corner-sharing  $KCl_6$  and  $BiCl_6$  octahedra.

Here, the variable-temperature crystal structures of **1** at 293 K and 373 K were determined by X-ray diffraction, revealing the structural feature related to the phase transition. At 293 K, in the low-temperature phase (LTP), **1** crystallizes in the trigonal

space group  $R\bar{3}m$  with cell parameters of  $a = b = 7.8314(2)$  Å,  $c = 20.9786(7)$  Å,  $V = 1114.26(7)$  Å<sup>3</sup> and  $Z = 3$ . The basic building units of **1** contain  $BiCl_6$  and  $KCl_6$  octahedra which form a 3D bimetal inorganic framework. Each  $BiCl_6$  unit connects with six K ions through six adjacent Cl atoms. The  $Bi^{3+}$  and  $K^+$  ions occupy different metal positions with distinct coordination environments. The corresponding distances for Bi–Cl bond lengths are 2.6791 Å and 2.6792 Å, which are shorter compared with the K–Cl bonds (3.047 Å). The Cl–Bi–Cl angles vary from 88.26° to 180° and the Cl–K–Cl angles vary from 81.69° to 180°, as compared to the ideal octahedral values of 90.00° and 180.00°. As a result, the corner-sharing  $KCl_6$  and  $BiCl_6$  octahedra show a distorted coordination geometry. Furthermore, the distorted cage,  $[K_4Bi_4Cl_{12}]$ , is irregular with Bi···K distances of 5.716 Å and Bi–Cl–K angles of 173.07° (Table S1, ESI†). The MA cation, remaining in an ordered state, is anchored in the cage by weak hydrogen bonds between the –Cl and –NH<sub>3</sub> groups with a Cl···N distance of 3.429 Å (Table S2, ESI†).

The high-temperature phase (HTP) **1**, at 373 K, undergoes a drastic structure change by crystallizing in the cubic space group  $Fm\bar{3}m$  with cell parameters of  $a = b = c = 11.4524(3)$  Å,  $V = 1502.07(12)$  Å<sup>3</sup> and  $Z = 2$ . It shows a perfect double-perovskite structure, that is, the  $Bi^{3+}$  and  $K^+$  ions have regular octahedral coordination. The values of Bi–Cl distances and K–Cl distances are 2.686 Å and 3.040 Å, respectively. In the basic anionic cage, the edge (Bi–Cl–K) has a length of 5.726 Å and the Bi–Cl–K angle is 180° (Table S1, ESI†). The MA cation resides in the cage, showing high disorder. This is very similar to the hybrid organic–inorganic double perovskite-type compound,  $(MA)_2[KCo(CN)_6]$ , in the high-temperature phase.<sup>6b</sup> For **1**, the models for the potential configurations of the MA in the cage-like anionic crystal include (i) face orientations ( $[100]$ ); (ii) edge orientations ( $[110]$ ); and (iii) corner orientations ( $[111]$ ). This fact is consistent with the phase transition revealed by the DSC measurements. Meanwhile, the model is generated after routine structure refinements and restrained C–N bonds (1.35 Å). Since the MA is located on the crystallographic axis, its state can be understood as disorder caused by rotation around the crystallographic axis. It is very common that in crystals especially metal–organic frameworks with spherical molecules, the molecular reorientations have relatively low activation energy, leading to dynamical disorder, which has been widely used in the design of molecule-based phase transition compounds.<sup>10</sup> Therefore, the occurrence of the structural phase transition is ascribed to the reorientation of the MA cation and the drastic structural changes of the anionic framework from heavily distorted to a regular cube cage.

### Dielectric properties of **1**

Dielectric properties are a basic attribute of all-dielectric materials, and are the macroscopic reflection of the electric polarization and movement of the electronic and ionic displacements inside the material under the action of the external electric field, temperature, stress, and so on.<sup>6,17</sup> It is known that the macroscopic physical quantity describing the internal electric polarization process of dielectric materials is the dielectric constant ( $\epsilon = \epsilon' - i\epsilon''$ , where  $\epsilon'$  is the real part and

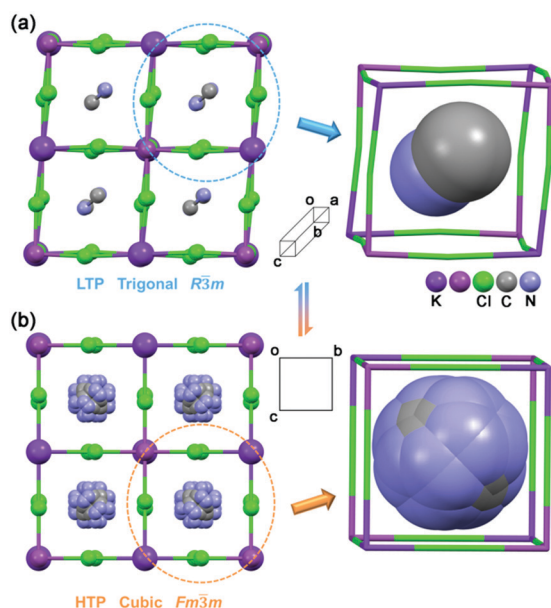
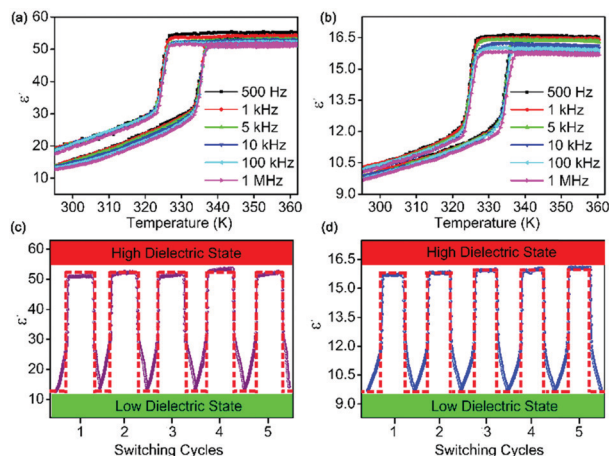


Fig. 2 Crystal structures of **1** at (a) LTP (293 K) and (b) HTP (373 K). The MA cations display a highly disordered state at HTP. Hydrogen atoms are omitted for clarity.





**Fig. 3** The variable-temperature dielectric constant measurement of **1** (a) the single-crystal sample [(001) direction, made perpendicular to the plate shown in Fig. S6, ESI†]. (b) The polycrystalline sample of **1**, showing extraordinary dielectric constant response and reversible dielectric constant switching activity between the low- and high-dielectric states. The dielectric switching measurement was through the temperature range of 323–343 K with a frequency of 1 MHz. Dielectric constant switching traces of (c) the single-crystal sample [(001) direction, made perpendicular to the plane shown in Fig. S1, ESI†] in the range of 323–343 K with a change rate of about  $1.7 \text{ K min}^{-1}$ . (d) The polycrystalline sample in the range of 323–343 K with a change rate of about  $1.3 \text{ K min}^{-1}$ . After several switching cycles, dielectric constant intensities recover rapidly without any obvious attenuation, showing highly switchable reversibility.

$\epsilon''$  is the imaginary part). Since the phase transition changes from trigonal to cubic, the symmetry mainly involves the change of the  $c$  axis. This indicates that the existing dielectric transition changes along the  $c$  axis, that is, perpendicular to the (001) plane. So, we oriented the monocrystalline samples to confirm the (001) plane (Fig. S6, ESI†). We measured the dielectric constant (fixed frequencies) to illustrate the structural phase transition caused by the internal order–disorder movement of **1**.

The dielectric constant of the single-crystal sample [(001) direction] shows obvious transition at 336/326 K (heating/cooling) measuring the temperature range from 293 K to 363 K, consistent with the DSC result, corresponding to the order–disorder structural phase transitions of **1** (Fig. 3a). The  $\epsilon'$  value of **1** is about 10.5 in the low-dielectric state at 1 MHz, while it rapidly increased to 51 in the high-dielectric state. The stepwise transition of the dielectric constant indicates that the relative internal molecular movement corresponds to the structural phase transition. Meanwhile, the dielectric constant measurements on crystalline-powdered samples of **1** were also validated (Fig. 3b). Although the dielectric switch behavior is similar, a strong dielectric anisotropy is recorded. Specifically, the large dielectric transition is found along the (001) direction.

Finally, we would like to discuss the reversibility of dielectric switching. It is very important to meet the needs of the application of dielectric materials. The stability of the dielectric switchable at 1 MHz upon the switching cycle measurements (Fig. 3c and d) is verified. It is clear that the intensity of the

$\epsilon'$  value retains the initial value and the transition rate of the dielectric almost remains unchanged. These results indicate that **1** has potential applications in dielectric materials.

## Conclusions

In conclusion, a bimetal halide hybrid double perovskite-type cage-like compound,  $(\text{MA})_2\text{KBiCl}_6$  (MA = methylammonium cation), was synthesized. Thermal analysis, variable temperature X-ray single-crystal diffraction, and dielectric measurements were used to characterize thermodynamic behavior. These results demonstrate that **1** undergoes an order–disorder reversible structural phase transition from trigonal ( $R\bar{3}m$ ) to cubic ( $Fm\bar{3}m$ ) at 336/326 K (heating/cooling). Furthermore, **1** is also a potential high-temperature dielectric switchable material because of its good endurance and suitable phase transition temperature. It is believed that this discovery will broaden the avenues to find outstanding rapid switchable dielectric materials.

## Conflicts of interest

There are no conflicts to declare.

## Acknowledgements

We sincerely thank Professor Xiao-Ying Huang (Fjirms) for his kind help with single crystal structure analysis. This work was supported by the National Natural Science Foundation of China (21805119 and 21875093), the Youth Science Foundation of Jiangxi Provincial Office of Science and Technology (20192ACBL21010) and the Natural Science Foundation of Jiangxi Province (20204BCJ22015 and 20202ACBL203001).

## References

- (a) Q. Pan, Z.-B. Liu, Y.-Y. Tang, P.-F. Li, R.-W. Ma, R.-Y. Wei, Y. Zhang, Y.-M. You, H.-Y. Ye and R.-G. Xiong, A Three-dimensional molecular perovskite ferroelectric: (3-Ammoniopyrrolidinium) $\text{RbBr}_3$ , *J. Am. Chem. Soc.*, 2017, **139**, 3954–3957; (b) W.-Y. Zhang, Y.-Y. Tang, P.-F. Li, P.-P. Shi, W.-Q. Liao, D.-W. Fu, H.-Y. Ye, Y. Zhang and R.-G. Xiong, Precise molecular design of high- $T_c$  3D organic-inorganic perovskite ferroelectric:  $[\text{MeHdabco}]\text{RbI}_3$  (MeHdabco = N-methyl-1,4-diazabicyclo[2.2.2]octane), *J. Am. Chem. Soc.*, 2017, **139**, 10897–10902; (c) H.-Y. Ye, Y.-Y. Tang, P.-F. Li, W.-Q. Liao, J.-X. Gao, X.-N. Hua, H. Cai, P.-P. Shi, Y.-M. You and R.-G. Xiong, Metal-free three-dimensional perovskite ferroelectrics, *Science*, 2018, **361**, 151–155.
- (a) Y. Wu, S. Shaker, F. Brivio, R. Murugavel, P. D. Bristowe and A. K. Cheetham,  $[\text{Am}]\text{Mn}(\text{H}_2\text{POO})_3$ : a new family of hybrid perovskites based on the hypophosphite ligand, *J. Am. Chem. Soc.*, 2017, **139**, 16999–17002; (b) Y. Wu, T. Binford, J. A. Hill, S. Shaker, J. Wang and A. K. Cheetham, Hypophosphite hybrid perovskites: a





- platform for unconventional tilts and shifts, *Chem. Commun.*, 2018, **54**, 3751–3754; (c) Y. Wu, D. M. Halat, F.-X. Wei, T. Binford, I. D. Seymour, M. W. Gaultois, S. Shaker, J. Wang, C. P. Grey and A. K. Cheetham, Mixed X-site formate-hypophosphite hybrid perovskites, *Chem. – Eur. J.*, 2018, **24**, 11309–11313; (d) H. A. Evans, Z.-Y. Deng, I. E. Collings, Y. Wu, J. L. Andrews, K. Pilar, J. M. Tuffnell, G. Wu, J. Wang, S. E. Dutton, P. D. Bristowe, R. Seshadri and A. K. Cheetham, Polymorphism in  $M(\text{H}_2\text{PO}_2)_3$  ( $M = \text{V}, \text{Al}, \text{Ga}$ ) compounds with the perovskite-related  $\text{ReO}_3$  structure, *Chem. Commun.*, 2019, **55**, 2964–2967; (e) H. A. Evans, Y. Wu, R. Seshadri and A. K. Cheetham, Perovskite-related  $\text{ReO}_3$ -type structures, *Nat. Rev. Mater.*, 2020, **5**, 196–213.
- 3 (a) B. Liu, R. Shang, K.-L. Hu, Z.-M. Wang and S. Gao, A new series of chiral metal formate frameworks of  $[\text{HONH}_3][\text{MII}(\text{HCOO})_3]$  ( $M = \text{Mn}, \text{Co}, \text{Ni}, \text{Zn}$ , and  $\text{Mg}$ ): synthesis, structures, and properties, *Inorg. Chem.*, 2012, **51**, 13363–13372; (b) S. Chen, R. Shang, K.-L. Hu, Z.-M. Wang and S. Gao,  $[\text{NH}_2\text{NH}_3][\text{M}(\text{HCOO})_3]$  ( $M = \text{Mn}^{2+}, \text{Zn}^{2+}, \text{Co}^{2+}$  and  $\text{Mg}^{2+}$ ): structural phase transitions, prominent dielectric anomalies and negative thermal expansion, and magnetic ordering, *Inorg. Chem. Front.*, 2014, **1**, 83–98; (c) S. Chen, R. Shang, B.-W. Wang, Z.-M. Wang and S. Gao, An A-site mixed-ammonium solid solution perovskite series of  $[(\text{NH}_2\text{NH}_3)_x(\text{CH}_3\text{NH}_3)_{1-x}][\text{Mn}(\text{HCOO})_3]$  ( $x = 1.00\text{--}0.67$ ), *Angew. Chem., Int. Ed.*, 2015, **54**, 11093–11096; (d) Y.-H. Zhao, S. Liu, B.-W. Wang, Z.-M. Wang and S. Gao, Three new niccolites: high-temperature phase transitions, prominent anisotropic thermal expansions, dielectric anomalies, and magnetism, *Chem. – Eur. J.*, 2019, **25**, 9303–9314.
- 4 (a) L.-H. Kong, D.-W. Fu, Q. Ye, H.-Y. Ye, Y. Zhang and R.-G. Xiong, Iso-structural phase transition in tetramethylammonium nickel(II) nitrite  $[(\text{CH}_3)_4\text{N}][\text{Ni}(\text{NO}_2)_3]$ , *Chin. Chem. Lett.*, 2014, **25**, 844–848; (b) Y.-A. Xiong, T.-T. Sha, Q. Pan, X.-J. Song, S.-R. Miao, Z.-Y. Jing, Z.-J. Feng, Y.-M. You and R.-G. Xiong, A nickel(II)-nitrite-based molecular perovskite ferroelectric, *Angew. Chem., Int. Ed.*, 2019, **58**, 8857–8861; (c) B.-B. Deng, C.-C. Xu, T.-T. Cheng, Y.-T. Yang, Y.-T. Hu, P. Wang, W.-H. He, M.-J. Yang and W.-Q. Liao, Homochiral nickel nitrite  $\text{ABX}_3$  ( $X = \text{NO}_2^-$ ) perovskite ferroelectrics, *J. Am. Chem. Soc.*, 2020, **142**, 6946–6950.
- 5 (a) M. Wojciechowska, A. Gagor, A. Piecha-Bisiorek, R. Jakubas, A. Cizman, J. K. Zareba, M. Nyk, P. Zielinski, W. Medycki and A. Bil, Ferroelectricity and ferroelasticity in organic inorganic hybrid (pyrrolidinium) $_3$  $[\text{Sb}_2\text{Cl}_6]$ , *Chem. Mater.*, 2018, **30**, 4597–4608; (b) M. Moskwa, G. Bator, M. Rok, W. Medycki, A. Miniewicz and R. Jakubas, Investigations of organic-inorganic hybrids based on homopiperidinium cation with haloantimonates(III) and halobismuthates(III). Crystal structures, reversible phase transitions, semiconducting and molecular dynamic properties, *Dalton Trans.*, 2018, **47**, 13507–13522; (c) M. Rok, P. Starynowicz, A. Cizman, J. K. Zareba, A. Piecha-Bisiorek, G. Bator and R. Jakubas, Advances and property investigations of an organic–inorganic ferroelectric: (diisopropylammonium) $_2$  $[\text{CdBr}_4]$ , *Inorg. Chem.*, 2020, **59**, 11986–11994.
- 6 (a) C. Shi, X. Zhang, Y. Cai, Y.-F. Yao and W. Zhang, A chemically triggered and thermally switched dielectric constant transition in a metal cyanide based crystal, *Angew. Chem., Int. Ed.*, 2015, **54**, 6206–6210; (b) C. Shi, C.-H. Yu and W. Zhang, Predicting and screening dielectric transitions in a series of hybrid organic-inorganic double perovskites via an extended tolerance factor approach, *Angew. Chem., Int. Ed.*, 2016, **55**, 5798–5802; (c) M. Trzebiatowska, M. Maczka, A. Gagor and A. Sieradzki, Pyrrolidinium-based cyanides: unusual architecture and dielectric switchability triggered by order-disorder process, *Inorg. Chem.*, 2020, **59**, 8855–8863; (d) M. Rok, A. Cizman, B. Zarychta, J. K. Zareba, M. Trzebiatowska, M. Maczka, A. Stroppa, S.-R. Yuan, A. E. Phillips and G. Bator, Cyano-bridged perovskite  $[(\text{CH}_3)_3\text{NOH}]_2[\text{KM}(\text{CN})_6]$ ,  $[\text{M}: \text{Fe}(\text{III}), \text{and Co}(\text{III})]$  for high-temperature multi-axial ferroelectric applications with enhanced thermal and nonlinear optical performance, *J. Mater. Chem. C*, 2020, **8**, 17491–17501.
- 7 (a) W.-Q. Guo, X.-T. Liu, S.-G. Han, Y. Liu, Z.-Y. Xu, M.-C. Hong, J.-H. Luo and Z.-H. Sun, Room-temperature ferroelectric material composed of a two-dimensional metal halide double perovskite for x-ray detection, *Angew. Chem., Int. Ed.*, 2020, **59**, 13879–13884; (b) L. Lu, X. Pan, J.-H. Luo and Z.-H. Sun, Recent advances and optoelectronic applications of lead-free halide double perovskites, *Chem. – Eur. J.*, 2020, **26**, 16975–16984; (c) X.-T. Liu, Z.-Y. Xu, P.-Q. Long, Y.-P. Yao, C.-M. Ji, L.-N. Li, Z.-H. Sun, M.-C. Hong and J.-H. Luo, A multiaxial layered halide double perovskite ferroelectric with multiple ferroic orders, *Chem. Mater.*, 2020, **32**, 8965–8970.
- 8 (a) Z.-Y. Deng, F.-X. Wei, F. Brivio, Y. Wu, S.-J. Sun, P. D. Bristowe and A. K. Cheetham, Synthesis and characterization of the rare-earth hybrid double perovskites:  $(\text{CH}_3\text{NH}_3)_2\text{KdCl}_6$  and  $(\text{CH}_3\text{NH}_3)_2\text{KYCl}_6$ , *J. Phys. Chem. Lett.*, 2017, **8**, 5015–5020; (b) L.-L. Mao, S. M. L. Teicher, C. C. Stoumpos, R. M. Kennard, R. A. DeCrescent, G. Wu, J. A. Schuller, M. L. Chabinyk, A. K. Cheetham and R. Seshadri, Chemical and structural diversity of hybrid layered double perovskite halides, *J. Am. Chem. Soc.*, 2019, **141**, 19099–19109.
- 9 (a) C. Shi, L. Ye, Z.-X. Gong, J.-J. Ma, Q.-W. Wang, J.-Y. Jiang, M.-M. Hua, C.-F. Wang, H. Yu, Y. Zhang and H.-Y. Ye, Two-dimensional organic-inorganic hybrid rare-earth double perovskite ferroelectrics, *J. Am. Chem. Soc.*, 2020, **142**, 545–551; (b) C. Shi, J.-J. Ma, J.-Y. Jiang, M.-M. Hua, Q. Xu, H. Yu, Y. Zhang and H.-Y. Ye, Large piezoelectric response in hybrid rare-earth double perovskite relaxor ferroelectrics, *J. Am. Chem. Soc.*, 2020, **142**, 9634–9641; (c) M.-M. Hua, L. Ye, Q.-W. Wang, J.-J. Ma, Z.-X. Gong, Q. Xu, C. Shi and Y. Zhang, A layered hybrid rare-earth double-perovskite-type molecule-based compound with electrical and optical response properties, *J. Mater. Chem. C*, 2020, **8**, 16349–16353.
- 10 (a) W. Zhang and R.-G. Xiong, Ferroelectric metal-organic frameworks, *Chem. Rev.*, 2012, **112**, 1163–1195; (b) C. Shi, X.-B. Han and W. Zhang, Structural phase



- transition-associated dielectric transition and ferroelectricity in coordination compounds, *Coord. Chem. Rev.*, 2019, **378**, 561–576.
- 11 W. Li, Z.-M. Wang, F. Deschler, S. Gao, R. H. Friend and A. K. Cheetham, Chemically diverse and multifunctional hybrid organic-inorganic perovskites, *Nat. Rev. Mater.*, 2017, **2**, 16099–16116.
  - 12 (a) D.-W. Fu, J.-X. Gao, W.-H. He, X.-Q. Huang, Y.-H. Liu and Y. Ai, High- $T_c$  enantiomeric ferroelectrics based on homochiral dabco-derivatives (dabco = 1,4-diazabicyclo[2.2.2]octane), *Angew. Chem., Int. Ed.*, 2020, **59**, 17477–17481; (b) Y.-F. Xie, Y. Ai, Y.-L. Zeng, W.-H. He, X.-Q. Huang, D.-W. Fu, J.-X. Gao, X.-G. Chen and Y.-Y. Tang, The soft molecular polycrystalline ferroelectric realized by the fluorination effect, *J. Am. Chem. Soc.*, 2020, **142**, 12486–12492; (c) D.-W. Fu, J.-X. Gao, P.-Z. Huang, R.-Y. Ren, T. Shao, L.-J. Han, J. Liu and J.-M. Gong, Observation of transition from ferroelasticity to ferroelectricity by solvent selective effect in anilinium bromide, *Angew. Chem., Int. Ed.*, 2021, **60**, 8198–8202.
  - 13 (a) L. He, P.-P. Shi, M.-M. Zhao, C.-M. Liu, W. Zhang and Q. Ye, Emergent chirality and nonlinear optical switching in a ferroelastic molecular perovskite solid solution, *Chem. Mater.*, 2021, **33**, 799–805; (b) L. He, P.-P. Shi, L. Zhou, Z.-B. Liu, W. Zhang and Q. Ye, Coexisting ferroelectric and ferroelastic orders in rare 3D homochiral hybrid bimetal halides, *Chem. Mater.*, 2021, **33**, 6233–6239.
  - 14 Y. S. Kim, M. Liu, Y. Ishida, Y. Ebina, M. Osada, T. Sasaki, T. Hikima, M. Takata and T. Aida, Thermoresponsive actuation enabled by permittivity switching in an electrostatically anisotropic hydrogel, *Nat. Mater.*, 2015, **14**, 1002–1007.
  - 15 F.-X. Wei, Z.-Y. Deng, S.-J. Sun, F. Xie, G. Kieslich, D. M. Evans, M. A. Carpenter, P. D. Bristowe and A. K. Cheetham, The synthesis, structure and electronic properties of a lead-free hybrid inorganic-organic double perovskite (MA)<sub>2</sub>KBiCl<sub>6</sub> (MA = methylammonium), *Mater. Horiz.*, 2016, **3**, 328–332.
  - 16 (a) H. Mashiyama, Y. Kawamura, H. Kasano, T. Asahi, Y. Noda and H. Kimura, Disordered configuration of methylammonium of CH<sub>3</sub>NH<sub>3</sub>PbBr<sub>3</sub> determined by single crystal neutron diffraction, *Ferroelectrics*, 2007, **348**, 584–588; (b) A. M. A. Leguy, J. M. Frost, A. P. McMahon, V. G. Sakai, W. Kockelmann, C.-H. Law, X.-E. Li, F. Foglia, A. Walsh, B. C. O'Regan, J. Nelson, J. T. Cabral and P. R. F. Barnes, The dynamics of methylammonium ions in hybrid organic-inorganic perovskite solar cells, *Nat. Commun.*, 2015, **6**, 7124–7133.
  - 17 C. Shi, X. Zhang, C.-H. Yu, Y.-F. Yao and W. Zhang, Geometric isotope effect of deuteration in a hydrogen-bonded host-guest crystal, *Nat. Commun.*, 2018, **9**, 481–489.

